

Bounds on quantum confinement effects in metal nanoparticles

G. Neal Blackman III and Dentcho A. Genov

College of Engineering and Science, Louisiana Tech University, Ruston, LA 71272, USA

(Dated: December 14, 2024)

Quantum size effects on the permittivity of metal nanoparticles are investigated using the quantum box model. Explicit upper and lower bounds are derived for the permittivity and relaxation rates due to quantum confinement effects. These bounds are verified numerically, and the size-dependence and frequency-dependence of the empirical Drude size parameter is extracted from the model. Results suggest that the common practice of empirically modifying the dielectric function can lead to inaccurate predictions for highly uniform distributions of finite-sized particles.

I. INTRODUCTION

Metallic nanostructures and their associated surface plasmon resonances (SPRs) enable incident light to be intensified by several orders of magnitude. This plasmonic enhancement plays a paramount role in a broad range of emerging optical technologies, including electromagnetic cloaks and metamaterials,¹⁻⁴ superlenses,⁵⁻⁷ ultrafast optoelectronics,⁸⁻¹⁰ cancer treatments,^{11,12} and sensitive chemical sensors.¹³⁻¹⁵ The mechanism of plasmonic enhancement has been well studied within the context of classical electrodynamics. However, as the feature size of nanomaterials approach atomic scale, quantum-mechanical effects emerge, which in some cases can further enhance their plasmonic properties. In this paper, we demonstrate that bounds can be placed on the additional effects due to quantum confinement.

The optical behavior of large metal nanoscale objects (> 10 nm) are described using bulk permittivity functions and classical electrodynamics methods such as Mie theory¹⁶ or the discrete-dipole approximation.¹⁷⁻¹⁹ Bulk permittivity functions of metals $\varepsilon(\omega) = \varepsilon_b(\omega) + \varepsilon_D(\omega)$ can be formally separated into the bound electron contribution $\varepsilon_b(\omega)$ and the conduction electron (Drude) contribution $\varepsilon_D(\omega)$ with the Drude component given by^{20,21}

$$\begin{aligned}\varepsilon_D(\omega) &= \varepsilon'_D(\omega) + i\varepsilon''_D(\omega) \\ &= 1 - \frac{\omega_p^2}{\omega^2 + \gamma^2} + i\frac{\omega_p^2\gamma}{\omega(\omega^2 + \gamma^2)},\end{aligned}\quad (1)$$

where γ is a phenomenological damping constant (relaxation rate), and $\omega_p = (n_e e^2 / \varepsilon_0 m_e)^{1/2}$ is the plasma frequency, which depends on the conduction electron density n_e , the electron charge e , and the effective electron mass m_e . For the majority of this work, we will focus on the conduction band contribution since it is dominant in the infrared and visible frequencies for many metals. We will revisit the bound electron component in the section dedicated to experimental comparison since it plays an important role in noble metals like silver, copper, and gold at frequencies close to the surface plasmon resonance.²²

Although Eq. (1) accurately describes the conduction electron behavior in bulk metals and large metal particles, experiments have shown that the relaxation rate γ is inversely proportional to the particle radius for small

particles.^{23,24} The proportionality constant is sensitive to a multitude of microscopic effects such as particle geometry, surface roughness, chemical interface effects, and energy level quantization (quantum confinement), all of which become significant when the particle size is less than 10 nm.^{25,26} It is common practice to incorporate these effects into Eq. (1) by introducing an empirical size parameter \mathcal{A} so that the relaxation rate is given by

$$\gamma(R) = \gamma_0 + \mathcal{A}\frac{v_F}{R} \quad (2)$$

where v_F is the Fermi velocity and γ_0 is the bulk value of the damping constant. Values reported for \mathcal{A} are of the order of one, but different theoretical approaches and experimental conditions have led to a wide range of values in the literature.^{26,27}

The $1/R$ contribution in Eq. (2) can be explained classically by the *free path effect*.²⁸ When a particle's dimensions are large, the damping constant is a size-independent material constant given by $\gamma_0 = v_F/l_\infty$, where l_∞ is the mean free path of electrons in the bulk metal. When a particle's dimensions are comparable to the bulk mean free path ($2R \approx l_\infty$), surface scattering decreases the effective mean free path. When surface collisions are included, classical calculations for spherical particles find Eq. (2) with either $\mathcal{A} = 1$ for diffuse scattering or $\mathcal{A} = 0.75$ for isotropic conditions.²⁹

Although classical theories^{28,30} can phenomenologically explain the experimentally-observed $1/R$ behavior in SPR broadening, classical theory has failed to reproduce the range of experimental values measured for the size parameter.^{24,26,27} Furthermore, classical theory ignores energy level quantization, which is expected to play a significant role in nano-sized structures. This has prompted the development of several quantum mechanical approaches. The most detailed include *ab initio* techniques and time-dependent (TD) density functional theory (DFT),^{31,32} but these methods are usually restricted to particles consisting of less than 120 atoms because of their computational demand.³³⁻³⁶ Some optimized techniques include less physical details and combine DFT with more efficient atomistic approaches, but even these methods are limited to particles smaller than $R \approx 2.5$ nm.³⁷⁻³⁹ To model larger particles, simpler quantum mechanical methods are required. These include the jellium model⁴⁰⁻⁴⁵ and the canonical particle-in-a-box model pi-

oneered by Kawabata and Kubo.⁴⁶

The primary advantage of the particle-in-a-box technique, referred to as the quantum box model (QBM), is that it uniquely allows for analytical solutions and closed-form expressions which provide more physical insight than purely numerical schemes. It is for this reason that the QBM has received extensive attention in the literature.^{30,46–59} We use the framework of the QBM to evaluate the limits to which quantum confinement of the conduction electrons can further enhance the optical properties of metal nanoparticles. We will focus primarily on damping effects since line-shape broadening is the most pronounced size-dependent effect for SPRs of metal particles in the $R = 1\text{--}10$ nm range.

In Sec. II we introduce the spherical QBM and summarize numerical calculations for finite-sized systems. The results are consistent with previous finite-size calculations,^{43,58,59} showing that the permittivity ε and the relaxation rate γ are characterized by a range of values that fluctuate sensitively with respect to frequency and particle size. We demonstrate that the Drude size parameter \mathcal{A} is similarly characterized by fluctuating values since it is directly linked to γ . Hence in Sec. III we derive analytical bounds on the fluctuations in these three related quantities, and we verify the analytical bounds using numerical calculations. Finally, in Sec. IV, we compare experimental measurements of the size parameter with numerical QBM calculations for non-uniform size distributions. Results point toward a different approach for treating the optical response of nano-sized metallic systems. Specifically, we argue in Sec. V that for highly uniform size distributions, either: (i) a quantum-mechanical permittivity calculation should be used, (ii) a frequency- and size-dependent function $\mathcal{A}(\omega, R)$ must be introduced, or (iii) the proper bounds should be used to calculate the range of expected optical properties.

II. QUANTUM BOX MODEL (QBM)

In the QBM, N conduction electrons are confined within an infinite potential well whose dimensions are designed to represent a particle of the same size. The electrons are assumed to be non-interacting, with each electron belonging to its own single-electron eigenstate. In a spherical well of radius R , the wavefunctions have the form $\psi_{nlm} = A_{nl} j_l(a_{nl}r/R) Y_l^m(\theta, \phi)$ where $A_{nl} = (2/R^3)^{1/2} / j_{l+1}(a_{nl})$ is the normalization constant, Y_l^m denotes the spherical harmonics ($-l \leq m \leq l$), and a_{nl} represents the n th zero of the spherical Bessel function j_l with order $l \geq 0$. These states have the energy levels $E_{nl} = \hbar^2 a_{nl}^2 / 2m_e R^2$ with degeneracy $g(E_{nl}) = 2l + 1$ and are presented in Fig. 1. The electromagnetic response of the conduction electrons is given by the standard quantum mechanical susceptibility tensor for linear

materials:⁶⁰

$$\chi^{ij}(\omega, R) = \frac{1}{\varepsilon_0 \hbar V} \sum_s \sum_{s'} \frac{(w_s - w_{s'}) \mu_{ss'}^i \mu_{s's}^j}{\omega_{ss'} - \omega - i\gamma_{ss'}/2}, \quad (3)$$

where w_s and $w_{s'}$ are the occupation numbers of the states $|s\rangle$ and $|s'\rangle$, $\omega_{ss'} = (E_{s'} - E_s)/\hbar$ is the transition frequency, V is the volume of the particle, and $\gamma_{ss'}$ is the transition relaxation rate. The electric dipole transition moments are given by $\mu_{ss'}^j = \langle s | e r_j | s' \rangle$ where r_j is the displacement in the direction of the polarization unit vector \hat{e}_j . Note that Eq. (3) does not include non-local effects, which are expected to play a role in very small particles^{61,62} and are best described by more detailed approaches like TDDFT. For this reason, we restrict our analysis to particles with $R > 1$ nm.

The temperature dependence of the occupation numbers is given by Fermi statistics

$$w_s = \frac{2}{e^{(E_s - E_F)/k_B T} + 1}, \quad (4)$$

where k_B is Boltzmann's constant, E_F is the Fermi energy, and the factor of two accounts for spin degeneracy of the electron. The Fermi energy can be considered a constant value for bulk material (ϵ_F^∞), but it should be treated as a size-dependent parameter for small particles when quantization of energy levels becomes important. We calculate the size-dependent Fermi energy $\epsilon_F(R)$ using an electron-counting process as follows. The energy levels are filled from the ground state upward until we have accounted for each of the nanoparticle's $N = n_e V$ conduction electrons. At this point, the size-dependent Fermi energy has been reached. A visualization of this process can be seen in Fig. 1 where $\epsilon_F(R)$ approaches the bulk value as the particle size increases.

At ambient temperatures, thermal energy fluctuations are of the order of $k_B T \approx 0.02$ eV, whereas typical energy level spacings in the particles we are studying are $\delta_E \approx 0.1$ eV or smaller. Therefore, in this work we take $T = 0$ K as a good approximation to the low temperature limit ($\delta_E \gg k_B T$), which further simplifies the calculations. In this case, all states below the Fermi energy ($E \leq \epsilon_F$) are occupied with $w_s = 2$, and all states with $E > \epsilon_F$ are unoccupied with $w_s = 0$. Therefore, at zero temperature, the permittivity $\varepsilon(\omega) = 1 + \chi(\omega)$ becomes a sum over occupied (o) and unoccupied (u) states

$$\varepsilon^{ij}(\omega, R) = 1 + \omega_p^2 \sum_s^o \sum_{s'}^u \frac{S_{ss'}^{ij}}{\omega_{ss'}^2 - \omega^2 - i\omega\gamma_{ss'}}, \quad (5)$$

where we have introduced the oscillator strengths $S_{ss'}^{ij} = 4m_e \omega_{ss'} \mu_{ss'}^i \mu_{s's}^j / \hbar N$, which satisfy the sum rule $\sum_{ss'} S_{ss'}^{ii} = 1$. As verification of the low-temperature approximation, calculations have also been performed at 300 K (not shown here), which reveal negligible differences to the calculations performed at absolute zero.

Because all directions are equivalent for spherical particles, we can choose the z -direction to coincide with the

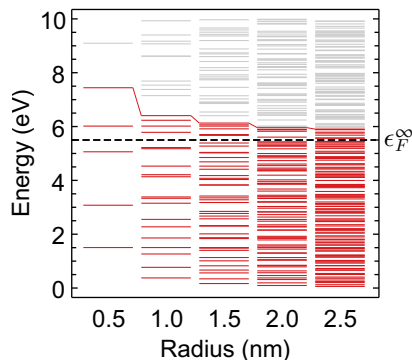


FIG. 1. (Color online) Energy levels of infinite spherical wells with varying radius, representing silver nanospheres with a constant electron density $n_e = 5.86 \times 10^{28} \text{ m}^{-3}$. Dark (red) lines indicate doubly occupied states at temperature $T = 0$ K, and light (gray) lines are unoccupied.

direction of polarization. The oscillator strengths $S_{ss'}^{zz} \equiv 4m_e\omega_{ss'} |\langle s|z|s'\rangle|^2 / \hbar N$ are then evaluated between the initial state $|s\rangle = |\psi_{nlm}\rangle$ and final state $|s'\rangle = |\psi_{n'l'm'}\rangle$. This leads to the selection rules $\Delta m = m' - m = 0$ and $\Delta l = l' - l = \pm 1$. Finally, the oscillator strengths for the allowed transitions are given by

$$S_{ss'}^{zz} = \delta_{\Delta m, 0} (C_{l+1}^m \delta_{\Delta l, 1} + C_l^m \delta_{\Delta l, -1}) \frac{16(a_{nl}a_{n'l'})^2}{N(a_{nl}^2 - a_{n'l'}^2)^3} \quad (6)$$

where $C_l^m = (l^2 - m^2)/(4l^2 - 1)$. Since the energy levels do not depend on the quantum number m , it essentially represents a degeneracy factor that can be incorporated into the strength factors. Thus it is convenient to define new oscillator strengths $S_{n,l,n',l'}^{zz} = \sum_{m=-l}^l S_{ss'}^{zz}$ that are independent of m . Evaluating the sum over m , we find

$$S_{n,l,n',l'}^{zz} = (\delta_{\Delta l, 1} + \delta_{\Delta l, -1}) \frac{16(a_{nl}a_{n'l'})^2(l+l'+1)}{3N(a_{n'l'}^2 - a_{nl}^2)^3}. \quad (7)$$

Eqs. (5) and (7) can then be used to write the permittivity as a sum over the quantum numbers n and l :

$$\begin{aligned} \varepsilon(\omega, R) = 1 + \frac{16\omega_p^2}{3N} \sum_{nl}^o \sum_{n'l'}^u \frac{(a_{nl}a_{n'l'})^2}{(a_{n'l'}^2 - a_{nl}^2)^3} \\ \times \frac{(\delta_{\Delta l, 1} + \delta_{\Delta l, -1})(l+l'+1)}{\omega_R^2(a_{n'l'}^2 - a_{nl}^2)^2 - \omega^2 - i\omega\gamma_0}, \quad (8) \end{aligned}$$

where we have defined the size-dependent frequency $\omega_R = \hbar/2m_eR^2$. In Eq. (8), we have suppressed the superscript z since the direction is unimportant, and we have fixed the transition relaxation rates to that of the bulk $\gamma_{ss'} = \gamma_0$. In reality, $\gamma_{ss'}$ represents the natural decay rate of the transitions, but no direct measurement has been made of this quantity, and so we have followed the common practice of relating it to the conductivity relaxation rate.^{26,54,63}

The sum in Eq. (8) is then evaluated numerically over all possible transitions from occupied states to unoccupied states until a reasonably high accuracy is achieved.⁵⁹

To monitor convergence, we enforced the sum rule with a very small tolerance $1 - \sum S_{ss'} < 10^{-4}$, which was achieved by including as many as 1.65 million transitions for the largest particle size considered in this study ($R = 20$ nm). Fewer transitions are required to achieve the same convergence for smaller particles.

Figs. 2(a,b) show the results for several sizes of silver nanoparticles. Both the real and imaginary parts approach bulk Drude behavior for large particles, but discrete resonances are prominent for smaller sizes. Quantum effects are easily seen in the infrared region of ε' where the QBM predicts that metal (silver) colloids/composites with particle sizes less than 2 nm should have dielectric behavior ($\varepsilon' > 0$) for electromagnetic radiation with wavelengths larger than 2 microns (0.6 eV). Size effects are also noticeable in the visible frequency range where a decrease in particle size leads to a rapid increase of ε'' and the appearance of strong resonances.

We now consider the relaxation phenomena as predicted by the QBM. In the optical frequency range, we can assume $\omega \gg \gamma$, in which case we can define an effective relaxation frequency in terms of the imaginary part of the permittivity $\gamma(\omega, R) = \omega^3 \varepsilon''(\omega, R) / \omega_p^2$. The effective size parameter then follows from Eq. (2) and is given by

$$\mathcal{A}(\omega, R) = \frac{\gamma(\omega, R) - \gamma_0}{v_F/R}. \quad (9)$$

The frequency dependence of $\mathcal{A}(\omega, R)$ for fixed particle sizes is presented in 2(c), showing that the QBM predicts values for the size parameter that fluctuate above and below the smooth asymptotic result due to Barma and Subrahmanyam (later improved by Yannouleas and Broglia).^{30,58} The common practice of extending the Drude model to be size-dependent $\varepsilon_D(\omega, R)$ by combining Eqs. (1) and (2) is only reasonable for high frequencies and large particle sizes where these deviations subside or when significant inhomogeneous broadening effects are present.

Considering that experimentally generated metal nanoparticle colloids and composite materials often consist of particles with sizes in the range of 1–10 nm, it is clear that quantum confinement effects are expected to play an important role for infrared and visible frequencies. In stark contrast to the semi-classical model, Fig. 2 demonstrates that a small change in particle size or frequency can drastically change the value of the optical functions and size parameter. This exemplifies the importance of gaining a better understanding of finite-size effects in nanoscopic systems. Accordingly, the following section is dedicated to deriving bounds on the fluctuations predicted by the QBM.

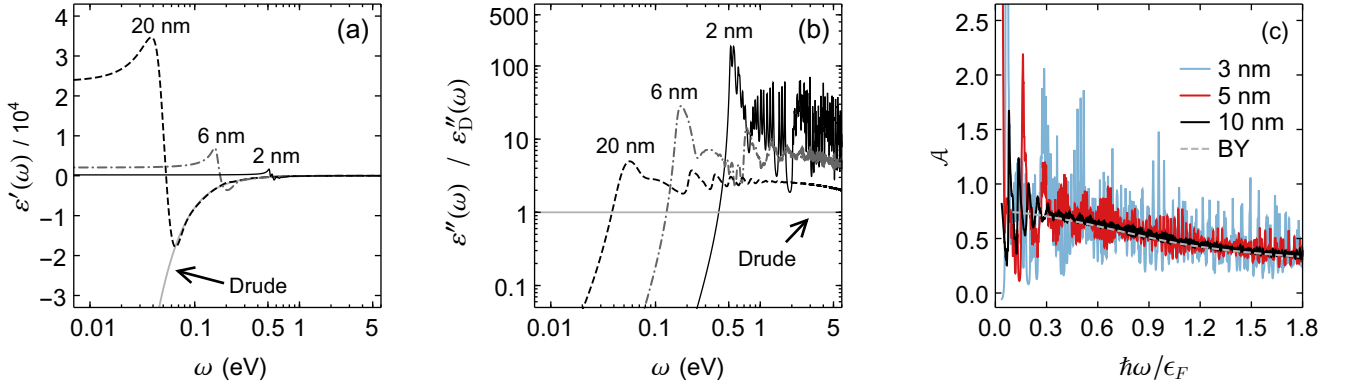


FIG. 2. The (a) real part and (b) imaginary part of the permittivity of silver nanospheres calculated using the QBM. Convergence to the bulk Drude function can be seen as particle size increases. (c) The frequency dependence of $\mathcal{A}(\omega, R)$ extracted from the QBM permittivity using Eq. (9). For comparison, the analytical result from Ref. 30 (BY) is shown in (c). Values used for silver were $\omega_p = 9.1$ eV, $\gamma_0 = 0.021$ eV, and $n_e = 5.86 \times 10^{28}$ m $^{-3}$ (constants acquired from Ref. 22 data).

III. ANALYTICAL BOUNDS ON THE PERMITTIVITY AND RELAXATION RATE

Previous authors have evaluated Eq. (8) or its equivalents by replacing summations with integrals,^{46,47,58} which in effect smooths the resonances and averages the values of Fig. 2. These smoothing techniques approximate highly disperse experimental samples, but they conceal the full potential of what might be detected experimentally. Hence we take a different approach by seeking explicit bounds on the resonance behavior so that a range of expected values can be estimated when calculating optical properties.

We begin by obtaining broad bounds on the particle permittivity given by Eq. (5) by minimizing and maximizing the summand with respect to $\omega_{ss'}$. The real part $\epsilon'(\omega)$ has a minimum at $\omega_{ss'} = \sqrt{\omega(\omega - \gamma_0)}$ and maximum at $\omega_{ss'} = \sqrt{\omega(\omega + \gamma_0)}$. The imaginary part $\epsilon''(\omega)$ has a maximum at $\omega_{ss'} = \omega$. Evaluating Eq. (5) under these conditions and applying the oscillator strength sum rule, we readily obtain the following bounds for the permittivity

$$-\frac{\omega_p^2}{2\omega\gamma_0} \leq \epsilon'(\omega) - 1 \leq \frac{\omega_p^2}{2\omega\gamma_0}, \quad 0 \leq \epsilon''(\omega) \leq \frac{\omega_p^2}{\omega\gamma_0}. \quad (10)$$

Although these bounds hold for all frequencies and particle sizes, they are not tight for high frequencies since they scale as $1/\omega$, which does not match the behavior of the Drude model for large ω ($\epsilon'_D \sim 1/\omega^2$ and $\epsilon''_D \sim 1/\omega^3$). Furthermore, it is of practical value to find size-dependent bounds that capture quantum size effects. In the remainder of this section we seek size-dependent bounds with Drude-like behavior so that we can better characterize the effects of quantum confinement.

Following a procedure similar to Kraus and Schatz,⁵⁴ we approximate the spherical Bessel zeros using $a_{nl} \approx \pi(n + 1 + l/2)$, which can be recognized as the leading term of McMahon's asymptotic formula⁶⁴ modified for

spherical Bessel zeros with $n \geq 0$. This is the simplest method that, as shown below, allows for obtaining tighter analytical bounds. McMahon's formula is exact for $l = 0$, so we define n_F as the value of the quantum number n on the Fermi surface when $l = 0$. With this definition, the Fermi energy is $\epsilon_F = \hbar\omega_R\pi^2(n_F + 1)^2$, and the Fermi surface is defined by the line $l = 2(n_F - n)$. Occupied states lie below this surface where $0 \leq n \leq n_F$, $0 \leq l \leq 2(n_F - n)$, and $-l \leq m \leq l$. Summing the occupied states and keeping only the leading term for large n_F , we find the relation between n_F and the number of states, $N_s = (4/3)n_F^3$. Taking the states to be doubly occupied ($N_s = N/2$) and inserting the approximate a_{nl} , the oscillator strengths follow from Eq. (7)

$$S_{ss'} = S_{n,l,\Delta n,\Delta l} \equiv (\delta_{\Delta l,1} + \delta_{\Delta l,-1}) \frac{8(2n+l+2)^2}{9n_F^3\pi^2(2\Delta n+\Delta l)^3} \times \frac{(2l+\Delta l+1)(2n+\Delta n+l+\Delta l+2)^2}{(4n+2\Delta n+2l+\Delta l+4)^3}. \quad (11)$$

Using the approximate energies $E_{nl} = \hbar^2\pi^2(n+1+l/2)^2/2m_eR^2$, the transition frequencies are

$$\omega_{n,l,\Delta n,\Delta l} \equiv \frac{\pi^2\omega_R}{4}(2\Delta n+\Delta l)(2\Delta n+\Delta l+4+2l+4n) \quad (12)$$

Therefore, the permittivity under the McMahon approximation is

$$\epsilon(\omega, R) = 1 + \omega_p^2 \sum_{\substack{n,l \\ \Delta n,\Delta l}} \frac{S_{n,l,\Delta n,\Delta l}}{\omega_{n,l,\Delta n,\Delta l}^2 - \omega^2 - i\omega\gamma_0}. \quad (13)$$

In writing Eqs. (11)-(13), we have used the transition notations $\Delta l = l' - l$ and $\Delta n = n' - n$. With this convention, the sum over states in Eq. (5) has become a sum over values of Δn and $\Delta l = \pm 1$ for which the occupied states transition to an unoccupied state. This leads to

the additional summation constraints

$$\Delta n \geq 1 - \frac{1 - \Delta l}{2} \quad (14a)$$

$$0 \leq n \leq n_F - \frac{1 - \Delta l}{2} \quad (14b)$$

$$l \geq \max \left[0, 2 \left(n_F - n - \Delta n + \frac{1 - \Delta l}{2} \right) \right] \quad (14c)$$

$$l \leq 2(n_F - n) \quad (14d)$$

At this point, the limits in Eq. (14) can be used to evaluate Eq. (13) for finite systems. However, the McMahon approximation is only valid when $n_F \gg 1$ (see Appendix A), so we only consider the limiting case of large n_F , which is also satisfied by our restriction $R > 1$ nm. When n_F is large, resonances with the same value of Δn begin to cluster together. As n_F increases, these individual resonances merge into collective resonances located at each group's average frequency $\omega_{\Delta n}$ found by summing over quantum numbers other than Δn

$$\omega_{\Delta n} \equiv \frac{1}{S_{\Delta n}} \sum_{n,l,\Delta l} S_{n,l,\Delta n,\Delta l} \omega_{n,l,\Delta n,\Delta l} = \omega_0(2\Delta n + 1) \quad (15)$$

where $\omega_0 = (\pi/2)v_F/R$. The group strength is found in a similar manner

$$S_{\Delta n} \equiv \sum_{n,l,\Delta l} S_{n,l,\Delta n,\Delta l} = \frac{8}{\pi^2(2\Delta n + 1)^2}. \quad (16)$$

Note that the group oscillator strengths $S_{\Delta n}$ satisfy the sum rule $\sum_{\Delta n=0}^{\infty} S_{\Delta n} = 1$, as they must. The specific details on the derivation of the group frequencies Eq. (15) and group oscillator strengths Eq. (16) are shown in Appendix A. For $n_F \gg 1$, the permittivity thus acquires the form of a single sum over Lorentzian resonances:

$$\varepsilon_{\infty}(\omega, R) = 1 + \omega_p^2 \sum_{\Delta n=0}^{\infty} \frac{S_{\Delta n}}{\omega_{\Delta n}^2 - \omega^2 - i\omega\gamma_0}. \quad (17)$$

The permittivity given by Eq. (17) has a closed-form solution $\varepsilon_{\infty}(\omega, R) = \varepsilon_D(\omega) + \varepsilon_s(\omega, R)$, where ε_D is the Drude permittivity [Eq. (1)], and ε_s is a finite-size contribution given by

$$\varepsilon_s(\omega, R) = \frac{2\omega_p^2\omega_0}{\pi\tilde{\omega}^3} \tan \left(\frac{\pi\tilde{\omega}}{2\omega_0} \right) \quad (18)$$

where $\tilde{\omega} \equiv \sqrt{\omega(\omega + i\gamma_0)}$. This result contains a continuum of resonances that broaden the lineshape of the optical response in a complex way. This exemplifies how applying the free path correction [Eq. (2)] to the bulk Drude function does not capture all of the relevant physics for very small particles. For larger objects, the finite-size contribution to the permittivity diminishes as $\varepsilon_s \sim 1/R$, and the permittivity is dominated by Drude behavior.

Although the result $\varepsilon_{\infty}(\omega, R)$ is an approximate solution to Eq. (8) for large particles, it can serve as the basis

for estimating bounds on the permittivity due to finite-size effects since it was constructed by clustering each Δn transition group into a single Lorentzian. Thus we assert that the minima and maxima of $\varepsilon_{\infty}(\omega, R)$ serve as true bounds on the original, unclustered band profile. This can be easily checked by a parametric sweep.

Bounds for the real part of the permittivity can be found by minimizing and maximizing the real part of Eq. (18). Written in terms of the Drude susceptibility $\chi'_D(\omega) = \varepsilon'_D(\omega) - 1$, we find

$$\begin{aligned} \chi'_D(\omega) \left(1 + \frac{2\omega_0}{\pi\omega} \operatorname{csch} \left(\frac{\pi\gamma_0}{2\omega_0} \right) \right) &\leq \varepsilon'(\omega, R) - 1 \leq \\ \chi'_D(\omega) \left(1 - \sqrt{1 + \frac{\omega_0^2}{\gamma_0^2} \left(1 + \frac{\pi^2\gamma_0^2}{12\omega_0} \right)} \right) &\end{aligned} \quad (19)$$

A lower bound for the imaginary part of the permittivity can be obtained by considering the $\Delta n = 0$ term in Eq. (17), and the upper bound for the imaginary part is found by maximizing the imaginary part of Eq. (18),

$$\begin{aligned} \frac{8\omega\gamma_0\omega_p^2/\pi^2}{(\omega_0^2 + \omega^2)^2 + (\omega\gamma_0)^2} &\leq \varepsilon''(\omega, R) \leq \\ \varepsilon''_D(\omega) \left(1 + \frac{2\omega_0}{\pi\gamma_0} \coth \left(\frac{\pi\gamma_0}{4\omega_0} \right) \right) &\end{aligned} \quad (20)$$

The detailed derivation of the bounds in Eqs. (19) and (20) are provided in Appendix B. Fig. 3 shows that the numerical calculation of $\varepsilon(\omega, R)$ contains resonances that fluctuate several orders of magnitude, but the resonances remain within the bounds given above. This has also been verified numerically with a complete parametric sweep from 0 to 10 eV for $1 \text{ nm} \leq R \leq 20 \text{ nm}$.

To better compare with free path effect calculations, we also consider bounding behavior for high frequencies ($\omega \gg \gamma_0$). In this case, we can write both upper and lower bounds with Drude-like behavior (see Appendix B, Section 4)

$$1 + \frac{2\omega_0}{\pi\gamma_0} \tanh \left(\frac{\pi\gamma_0}{4\omega_0} \right) \leq \frac{\varepsilon''(\omega, R)}{\varepsilon''_D(\omega)} \leq 1 + \frac{2\omega_0}{\pi\gamma_0} \coth \left(\frac{\pi\gamma_0}{4\omega_0} \right).$$

Because the imaginary part of the Drude permittivity can be written $\varepsilon''_D \approx \omega_p^2\gamma/\omega^3$ for $\omega \gg \gamma_0$, we can write the high-frequency bounds as $\omega_p^2\tilde{\gamma}_L/\omega^3 \leq \varepsilon''(\omega, R) \leq \omega_p^2\tilde{\gamma}_U/\omega^3$ where we have introduced the upper and lower bounds of the effective relaxation frequency

$$\tilde{\gamma}_L = \gamma_0 + \frac{v_F}{R} \tanh \left(\frac{R\gamma_0}{2v_F} \right) \quad (21)$$

$$\tilde{\gamma}_U = \gamma_0 + \frac{v_F}{R} \coth \left(\frac{R\gamma_0}{2v_F} \right) \quad (22)$$

Comparing with Eq. (2), we can also write Eqs. (21) and (22) as bounds on the size parameter

$$\tanh \left(\frac{\gamma_0 R}{2v_F} \right) \leq \mathcal{A}(R) \leq \coth \left(\frac{\gamma_0 R}{2v_F} \right). \quad (23)$$

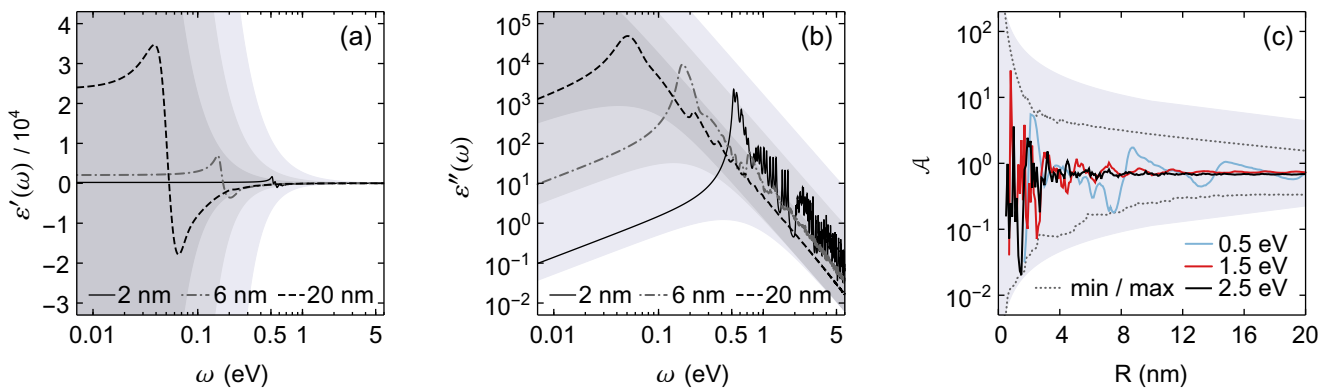


FIG. 3. Bounds on (a) the real part of the QBM permittivity, (b) the imaginary part of the QBM permittivity, and (c) the size parameter extracted from the QBM permittivity using Eq. (9). The shaded regions in (a) represent the bounds given by Eq. (19), and the shaded regions in (b) represent the bounds in Eq. (20), ranging from $R = 2$ nm (lightest) to $R = 20$ nm (darkest). The shaded region in (c) is given by Eq. (23). All quantities were evaluated for silver particles.

These analytical bounds are compared with the exact QBM calculation in Fig. 3(c) where effective values of \mathcal{A} have been extracted from $\varepsilon''(\omega, R)$ using Eq. (9) at three different frequencies. The values fall within the shaded area, which represent the high-frequency bounds given by Eq. (23). The tightest possible bounds for $\mathcal{A}(R)$ are the minimum and maximum values of $\mathcal{A}(\omega, R)$ for the frequency range $[\omega_1(R), \omega_M]$ where the lower limit $\omega_1(R)$ indicates the first transition frequency for a given particle radius, and the upper limit $\omega_M = 10$ eV is chosen to be sufficiently large such that $\omega_M \gg \omega_1(R)$ for $R > 1$ nm. Clearly, the true value of \mathcal{A} is frequency-dependent and fluctuates between the minimum and maximum values indicated by the dotted lines in Fig. 3(c). The range of values for $\mathcal{A}(R)$ becomes significantly wide even for $R \approx 5$ nm and continues to widen for smaller particle sizes, demonstrating that the semi-classical model is highly inaccurate for metal nanoparticles with diameters less than 10 nm. For particles in this size range, a quantum-mechanical result like Eq. (8) is more appropriate.

The fluctuations visible in Fig. 2 and Fig. 3 are similar to the oscillatory behavior reported by others.^{42–44,59,65} In experiments with inhomogeneous broadening effects such as size dispersion or surface roughness, these fluctuations may be smoothed out sufficiently that it is suitable to use average values of the optical functions. But for measurements performed on highly uniform particle samples or on individual nano-objects, this highly oscillatory behavior will remain. In these situations, bounds like the ones shown in Fig. 3 can be used to estimate a range of possible values.

IV. COMPARISON WITH EXPERIMENT

From the previous two sections, it is clear that quantum confinement can lead to large fluctuations in the permittivity and relaxation rates of finite-sized metal

nanoparticles. Such large fluctuations frequently go undetected experimentally due to the presence of additional inhomogeneous broadening effects in existing experimental techniques. In this section, we study how a non-uniform size distribution of particles can suppress these fluctuations and how differences in sample dispersity may explain discrepancies between different experiments.

In what follows we use published experimental data for silver nanoparticles embedded in glass.^{24,66} The experiments consider the broadening of the surface plasmon resonance in the absorption spectra and extract the effective permittivity of the particles. Since in the experiments the metal particles are not uniform in size, to compare with the theory we must perform averaging over a proper size distribution function $f(r, R, \sigma)$ with mean particle radius R and standard deviation σ . The effective particle permittivity ε_p is then obtained through the averaged polarizability using the Maxwell-Garnett theory

$$\frac{\bar{\varepsilon}_p(\omega, R, \sigma) - \varepsilon_m}{\bar{\varepsilon}_p(\omega, R, \sigma) + 2\varepsilon_m} = \int_0^\infty f(r, R, \sigma) \frac{\varepsilon_p(\omega, R) - \varepsilon_m}{\varepsilon_p(\omega, R) + 2\varepsilon_m} dr. \quad (24)$$

where $\varepsilon_p(\omega, R)$ is permittivity of a particle with fixed radius R , and ε_m is the permittivity of the embedding medium. Since the experimental data provides the values of the bound electron contribution to the permittivity ε_b , we can use Eq. (24) to extract the effective conduction electron permittivity $\varepsilon_D(\omega, R) = \varepsilon_p(\omega, R) - \varepsilon_b$ and hence the relaxation rate and size parameter according to Eq. (9). The values of the bound electron permittivity according to each experiment and the classical source used in our theoretical calculations, Johnson and Christy,²² are shown in Table I.

Fig. 4 shows the experimental data compared with calculations of normally distributed particle samples using $f(r, R, \sigma) = \exp(-(r - R)^2 / (2\sigma^2)) / \sqrt{2\pi\sigma^2}$. The values were calculated at the surface plasmon frequency of silver nanoparticles in glass in correspondence with the experimental conditions ($\omega_{sp} = 3.12$ eV). The calculations

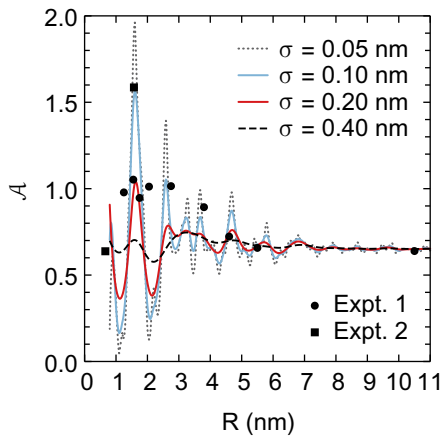


FIG. 4. The size parameter of silver nanoparticles embedded in glass ($\varepsilon_m = 2.3$). Theoretical values (lines) were calculated for normal size distributions using the QBM with effective medium theory [see Eq. (24)]. Values obtained from experimental data is also shown from Ref. 24 (Expt. 1) and Ref. 66 (Expt. 2). All values were calculated at the resonance frequency of silver particles in glass ($\omega_{sp} = 3.12$ eV).

predict significant fluctuations in the size parameter for small particles ($R < 5$ nm), whereas the size parameter quickly collapses to a constant value for larger particle sizes. The size-dependent fluctuations disappear almost entirely even for a relatively narrow size distribution with $\sigma = 0.4$ nm. The experimental values fall within the range of values predicted by the QBM. Varying the dispersity (σ) of the sample can also explain the variation in the data points.

The usage of the finite-size correction in Eq. (2) is widespread. Fig. 4 provides insight into its applicability for many realistic samples of metal particles since most current experimental techniques are limited to measurements on a sample with varying size, shape, and orientation. The necessity of quantum corrections to Eq. (2) depends strongly on both the average size and the dispersity of the sample. Because non-uniform particle samples suppress almost all quantum effects, extremely narrow size distributions are required to reliably test the predictions of the QBM.

TABLE I. Values used for interband correction, taken from experimental measurements on bulk silver at the resonance frequency for silver in glass ($\omega_{sp} = 3.12$ eV)

Ref.	ε'_b	ε''_b
Johnson and Christy ²²	4.19	0.15
Kreibig et al. ²⁴	4.38	0.24
Hilger ⁶⁶	4.20	0.90

V. CONCLUSION

In this work we performed a detailed study of size effects in the permittivity of metal nanoparticles using the quantum box model. By deriving strict analytical bounds on the permittivity, relaxation rates, and semi-classical size parameter \mathcal{A} , we investigated the limits to which quantum confinement effects can enhance their optical properties. We also argue that caution should be exercised when following the common practice of modeling finite-sized systems with a modified Drude function and Eq. (2). Quantum effects should be accounted for in uniform samples with particles smaller than 10 nm by either (i) using a quantum-mechanical permittivity like Eq. (8), (ii) studying proper bounds on the permittivity like Eqs. (19) and (20), or (iii) introducing a size-dependent and frequency-dependent function $\mathcal{A}(\omega, R)$.

Finally, by comparing the theory with experimental data, we provide an example of how a non-uniform size distribution can suppress the effects of quantum confinement. This can also explain the variance in measured values of the Drude size parameter \mathcal{A} , even when the measurements are performed under similar experimental conditions. Future experiments on highly uniform particle samples or even single nano-objects are needed to adequately test the size-dependent oscillatory behavior predicted by the QBM.

Appendix A: Evaluation of the McMahon sum rule

The exact sum rule $\sum_{ss'} S_{ss'} = 1$ is quite generally valid; however, the asymptotic McMahon approximation $a_{nl} \approx \pi(n + 1 + l/2)$ is only accurate when $n \gg l$, and it is not obvious that the sum rule is satisfied under this approximation. Here we demonstrate that the sum rule is indeed satisfied in the limit of large particle sizes ($n_F \gg 1$).

We start by noting that the limits in (14a-d) are the same for the two $\Delta l = \pm 1$ cases if we apply the transformation $\Delta n \rightarrow \Delta n + 1$ when $\Delta l = -1$ and assume $n_F \gg 1$. We can thus combine both Δl terms and use Eq. (11) to define a combined strength factor $T_{n,l,\Delta n} = S_{n,l,\Delta n+1,\Delta l=-1} + S_{n,l,\Delta n,\Delta l=+1}$ given by

$$T_{n,l,\Delta n} \equiv \frac{16(2n_F - l + 2)^2}{\pi^2 n_F^3 (2\Delta n + 1)^3} \times \frac{(4n_F - 2l - 4n + 1)(2\Delta n - l + 2n_F + 3)^2}{(2\Delta n - 2l + 4n_F + 5)^3}.$$

In writing $T_{n,l,\Delta n}$, we also applied the simplifying transformation $l \rightarrow -l + 2(n_F - n)$ and used the relation $N_s = (4/3)n_F^3$, which is the correct density of states for the McMahon approximation. Others have pointed out^{30,47,58} that the McMahon density of states does not agree with the bulk density of states, but we use the McMahon relation so that the model remains self-consistent.

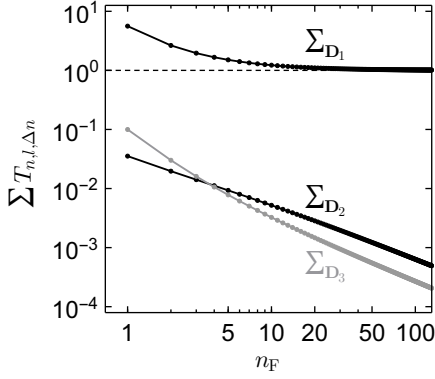


FIG. 5. Evaluation of the sum rule for the three different domains defined in Appendix A.

We define the set $\mathbf{D}(n, l, \Delta n) = \{n, l, \Delta n\}$ as the set of values n , l , and Δn which satisfy the summation constraints in (14a-d) with the transformations described in the previous paragraph. With these conditions, we can write the set \mathbf{D} as the union of three subsets, $\mathbf{D} = \mathbf{D}_1 \cup \mathbf{D}_2 \cup \mathbf{D}_3$, where we define the subsets by

\mathbf{D}_1	\mathbf{D}_2	\mathbf{D}_3
$0 \leq \Delta n \leq n_F$	$0 \leq \Delta n \leq n_F$	$\Delta n > n_F$
$0 \leq n \leq n_F - \Delta n$	$n_F - \Delta n < n \leq n_F$	$0 \leq n \leq n_F$
$0 \leq l \leq 2\Delta n$	$0 \leq l \leq 2(n_F - n)$	$0 \leq l \leq 2(n_F - n)$

The sum rule can then be written $\sum_{ss'} S_{ss'} = \sum_{\mathbf{D}} T_{n,l,\Delta n} = \sum_{\mathbf{D}_1} T_{n,l,\Delta n} + \sum_{\mathbf{D}_2} T_{n,l,\Delta n} + \sum_{\mathbf{D}_3} T_{n,l,\Delta n}$. From Fig. 5, it's clear that the sums over \mathbf{D}_2 and \mathbf{D}_3 vanish when n_F is large, so we have $\sum_{\mathbf{D}} T_{n,l,\Delta n} \simeq \sum_{\mathbf{D}_1} T_{n,l,\Delta n}$ for large n_F . If we write the upper summation limit for n assuming that $n_F \gg \Delta n$, then we find the group oscillator strengths

$$S_{\Delta n} \equiv \lim_{n_F \rightarrow \infty} \sum_{l=0}^{2\Delta n} \sum_{n=0}^{n_F} T_{n,l,\Delta n} = \sum_{l=0}^{2\Delta n} \frac{8}{\pi^2 (2\Delta n + 1)^3} = \frac{8}{\pi^2 (2\Delta n + 1)^2} \quad (\text{A1})$$

where we first performed the straightforward sum over n and subsequently applied the limit $n_F \rightarrow \infty$. The final sum over l can then be evaluated easily. The sum rule $\sum_{\Delta n=0}^{\infty} S_{\Delta n} = 1$ is readily verified, confirming that the sum rule is satisfied for $n_F \gg 1$.

The group frequencies are evaluated analogously to the sum rule. Combining $\omega_{n,l,\Delta n,\Delta l}$ for both $\Delta l = \pm 1$ terms and again applying the transformation $l \rightarrow -l + 2(n_F - n)$, we find

$$\Omega_{n,l,\Delta n} \equiv \frac{\hbar\pi^2}{8MR^2} (2\Delta n + 1)(2\Delta n - 2l + 4n_F + 5)$$

For large n_F we again only need to consider the sum corresponding to \mathbf{D}_1 , and the group average frequency becomes

$$\omega_{\Delta n} \equiv \frac{1}{S_{\Delta n}} \sum_{l=0}^{2\Delta n} \sum_{n=0}^{n_F} T_{n,l,\Delta n} \Omega_{n,l,\Delta n}$$

Keeping only the leading n_F term, we find

$$\omega_{\Delta n} = \frac{\hbar\pi^2 n_F}{2MR^2} (2\Delta n + 1) = \omega_0 (2\Delta n + 1) \quad (\text{A2})$$

where we have defined the characteristic frequency $\omega_0 \equiv \hbar\pi^2 n_F / 2MR^2 = (\pi/2)v_F/R$.

Appendix B: Bounds on the permittivity

We are ultimately interested in bounds for $\varepsilon_{\infty}(\omega, R)$. We first recast the problem in a more illuminating form by extracting the Drude term from the sum in Eq. (17). We can then split the finite-size contribution into its real and imaginary parts by writing

$$\text{Re}[\varepsilon_{\infty}(\omega)] - 1 = \chi'_D(1 + \xi(\nu, \tau)) \quad (\text{B1})$$

$$\text{Im}[\varepsilon_{\infty}(\omega)] = \chi''_D(1 + \eta(\nu, \tau)) \quad (\text{B2})$$

where we have defined the parameters $\nu = \omega/\omega_0$ and $\tau = \gamma/\omega_0$. In this form, the scaling functions $\xi(\nu, \tau)$ and $\eta(\nu, \tau)$ represent corrections to the Drude susceptibility functions χ'_D and χ''_D . The scaling functions are given by

$$\xi(\nu, \tau) = \frac{8}{\pi^2} \sum_{n=0}^{\infty} \frac{\nu^2 - \tau^2 - 1 - 4n(n+1)}{((2n+1)^2 - \nu^2)^2 + \nu^2\tau^2} \quad (\text{B3})$$

$$\eta(\nu, \tau) = \frac{8}{\pi^2} \sum_{n=0}^{\infty} \frac{2\nu^2 - (2n+1)^2}{((2n+1)^2 - \nu^2)^2 + \nu^2\tau^2} \quad (\text{B4})$$

The problem is now reduced to finding bounds for the functions ξ and η . The summations in (B3) and (B4) have the closed-form solutions $\xi(\nu, \tau) = -\text{Re}[f(\nu, \tau)]/\nu$ and $\eta(\nu, \tau) = \text{Im}[f(\nu, \tau)]/\tau$ where

$$f(\nu, \tau) = \frac{2(\nu - i\tau)^{3/2} \tan\left(\frac{\pi}{2} \sqrt{\nu(\nu + i\tau)}\right)}{\pi \sqrt{\nu(\nu^2 + \tau^2)}} \quad (\text{B5})$$

is a complex-valued function. In order to investigate the bounding behavior of these functions, we write Eq. (B5) entirely in terms of real-valued functions. Making use of the property $\tan(x + iy) = (\sin(2x) + i \sinh(2y)) / (\cos(2x) + \cosh(2y))$, we can write $f(\nu, \tau) = -F(\nu, \tau) + iG(\nu, \tau)$ where

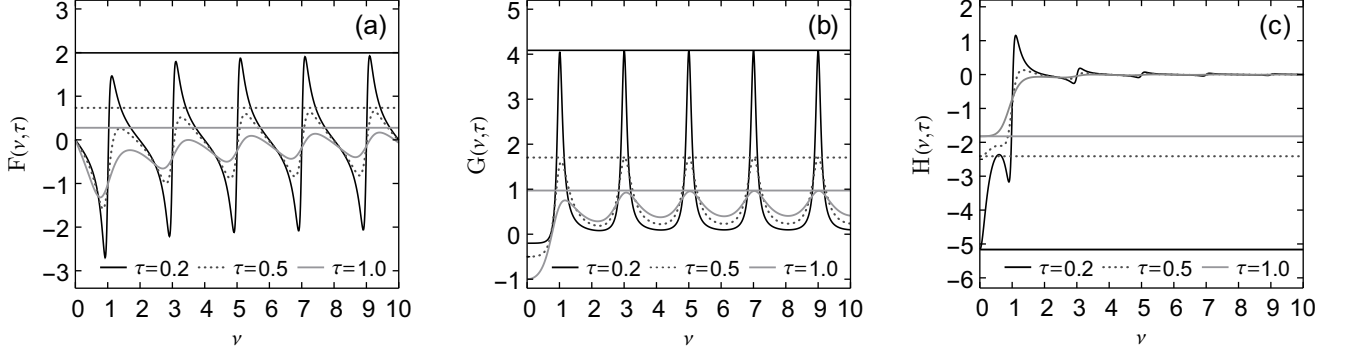


FIG. 6. The regularized scaling functions (a) $H(\nu, \tau) = (\nu\sqrt{\nu^2 + \tau^2})^{-1}F(\nu, \tau)$, (b) $F(\nu, \tau)$, and (c) $G(\nu, \tau)$ defined in Appendix B. Horizontal lines indicate limiting values. Global minima for $H(\nu, \tau)$ occurring at $\nu = 0$ are shown, and the global maxima of the functions $F(\nu, \tau)$ and $G(\nu, \tau)$ as $\nu \rightarrow \infty$ are shown for different values of τ .

$$F(\nu, \tau) = \frac{2Y(Y^2 - 3X^2) \sinh(\pi\nu Y) - 2X(X^2 - 3Y^2) \sin(\pi\nu X)}{\pi(X^2 + Y^2)(\cos(\pi\nu X) + \cosh(\pi\nu Y))} \quad (\text{B6})$$

$$G(\nu, \tau) = \frac{2Y(Y^2 - 3X^2) \sin(\pi\nu X) + 2X(X^2 - 3Y^2) \sinh(\pi\nu Y)}{\pi(X^2 + Y^2)(\cos(\pi\nu X) + \cosh(\pi\nu Y))} \quad (\text{B7})$$

with $X \equiv (1/\sqrt{2})\sqrt{1 + \sqrt{1 + (\tau/\nu)^2}}$ and $Y \equiv (1/\sqrt{2})\sqrt{-1 + \sqrt{1 + (\tau/\nu)^2}}$.

The scaling functions are thus $\xi(\nu, \tau) = F(\nu, \tau)/\nu$ and $\eta(\nu, \tau) = G(\nu, \tau)/\tau$. We now use the results (B6) and (B7) to seek the upper and lower bounds $\xi^- \leq \xi \leq \xi^+$ and $\eta^- \leq \eta \leq \eta^+$. The corresponding bounds on the permittivity are as follows

$$\chi'_D(1 + \xi^+) \leq \varepsilon' - 1 \leq \chi'_D(1 + \xi^-) \quad (\text{B8})$$

$$\varepsilon''_D(1 + \eta^-) \leq \varepsilon'' \leq \varepsilon''_D(1 + \eta^+) \quad (\text{B9})$$

Where possible, we explore frequency-independent bounds $\xi^-(\tau)$, $\xi^+(\tau)$, $\eta^-(\tau)$, and $\eta^+(\tau)$ in order to preserve the frequency dependence of the Drude functions in the bounds (B8) and (B9) above.

1. Lower bound for $\xi(\nu, \tau)$

It can be readily verified that the global minimum of $\xi(\nu, \tau)$ is always located in the range $0 \leq \nu_{\min} \leq 1$. However, the exact value of ν_{\min} depends on τ in a non-trivial way. We instead consider the function $H(\nu, \tau) \equiv (\nu^2 + \tau^2)^{-1/2}\xi(\nu, \tau) = (\nu\sqrt{\nu^2 + \tau^2})^{-1}F(\nu, \tau)$ shown in Fig. 6(a). This function is minimized at $\nu = 0$ for all values of τ , and the minimum value can be found by taking the limit as ν goes to zero:

$$\lim_{\nu \rightarrow 0} (\nu^2 + \tau^2)^{-1/2}\xi(\nu, \tau) = -\left(\frac{1}{\tau} + \frac{\pi^2\tau}{12}\right)$$

Since this is a minimum value, we can use it to write a frequency-dependent lower bound $\xi(\nu, \tau) \geq \xi^-(\nu, \tau)$ with

$$\xi^-(\nu, \tau) \equiv -(\nu^2 + \tau^2)^{1/2} \left(\frac{1}{\tau} + \frac{\pi^2\tau}{12}\right). \quad (\text{B10})$$

The bound $\xi^-(\nu, \tau)$ holds for all values of ν , so it must also be true that $\xi(\nu, \tau) \geq \xi^-(\nu_{\min}, \tau)$. Since we always have $\nu_{\min} \leq 1$ for $\xi(\nu, \tau)$, we can also establish a frequency-independent bound by evaluating Eq. (B10) at $\nu = 1$

$$\xi^-(\tau) \equiv -(1 + \tau^2)^{1/2} \left(\frac{1}{\tau} + \frac{\pi^2\tau}{12}\right). \quad (\text{B11})$$

2. Upper bound for $\xi(\nu, \tau)$

Observe in Fig. 6(b) that the function $\nu\xi(\nu, \tau) = F(\nu, \tau)$ has an infinite set of local maxima and minima which always monotonically increase to an asymptotic value. The limiting value can be found from the asymptotic behavior for $\nu \gg \tau$, in which case $X \approx 1$ and $Y \approx \tau/2\nu$. Dropping terms containing τ/ν , we obtain

$$F(\nu, \tau) \sim \frac{-2 \sin(\pi\nu)}{\pi \cos(\pi\nu) + \pi \cosh(\pi\tau/2)}, \quad (\nu \gg \tau). \quad (\text{B12})$$

This function has minima and maxima at $\nu_{\min, \max} = 2n \pm \arccos(-\text{sech}(\pi\tau/2))$. Evaluating (B12) at these

points, we find that the function asymptotically oscillates between two limiting values,

$$\lim_{\nu \rightarrow \infty} F(\nu, \tau) = \left[-\frac{2}{\pi} \operatorname{csch}\left(\frac{\pi\tau}{2}\right), \frac{2}{\pi} \operatorname{csch}\left(\frac{\pi\tau}{2}\right) \right]$$

Because the maxima of $F(\nu, \tau)$ increase monotonically, the positive asymptotic value must be an upper bound for all frequencies. Therefore, we have $\xi(\nu, \tau) \leq \xi^+ \equiv (2/\pi\nu) \operatorname{csch}(\pi\tau/2)$.

3. Lower bound for $\eta(\nu, \tau)$

The function $\eta(\nu, \tau)$ has a global minimum $\eta(0, \tau) = -1$. This establishes the bound $\varepsilon'' \geq \chi_D''$, which simply confirms that the imaginary part of the finite-size contribution ε_s'' is always positive. A tighter lower bound for ε'' can be found by instead considering the summation in Eq. (17). Since each imaginary term is always positive, every Δn term is a lower bound. We give the result for the first term ($\Delta n = 0$) in Eq. (20).

4. Upper and high-frequency bounds for $\eta(\nu, \tau)$

The function $G(\nu, \tau)$ has monotonically increasing maxima, so we again find the high-frequency asymptotic

for $\nu \gg \tau$. Taking $X \approx 1$ and $Y \approx \tau/2\nu$, we find

$$G(\nu, \tau) \sim \frac{2 \sinh(\pi\tau/2)}{\pi\tau \cos(\pi\nu) + \pi\tau \cosh(\pi\tau/2)} \quad (\text{B13})$$

Maximizing/minimizing with respect to ν , we find that minima occur at $\nu_{\min} = 2n$ and maxima at $\nu_{\max} = 2n+1$. The corresponding values are

$$\lim_{\nu \rightarrow \infty} G(\nu, \tau) = \left[\frac{2}{\pi} \tanh\left(\frac{\pi\tau}{4}\right), \frac{2}{\pi} \coth\left(\frac{\pi\tau}{4}\right) \right] \quad (\text{B14})$$

The lower value is a high frequency bound, but the upper value holds as a bound for all frequencies. Thus, we can conclude that $\eta(\nu, \tau) \leq \eta^+ \equiv (2/\pi\tau) \coth(\pi\tau/4)$ for all ν , and $\eta(\nu, \tau) \geq \eta^- \equiv (2/\pi\tau) \tanh(\pi\tau/4)$ for $\nu \gg \tau$.

ACKNOWLEDGMENTS

This work was supported by the NSF EPSCoR CIMM project under award #OIA-1541079 and the Louisiana Board of Regents.

-
- ¹ J. B. Pendry, D. Schurig, and D. R. Smith, *Science* **312**, 1780 (2006).
² U. Leonhardt, *Science* **312**, 1777 (2006).
³ W. Cai, U. K. Chettiar, A. V. Kildishev, and V. M. Shalaev, *Nat. Photonics* **1**, 224 (2007).
⁴ V. M. Shalaev, *Nat. Photonics* **1**, 41 (2007).
⁵ J. B. Pendry, *Phys. Rev. Lett.* **85**, 3966 (2000).
⁶ W. Cai, D. A. Genov, and V. M. Shalaev, *Phys. Rev. B* **72**, 193101 (2005).
⁷ R. B. Nielsen, M. D. Thoreson, W. Chen, A. Kristensen, J. M. Hvam, V. M. Shalaev, and A. Boltasseva, *Appl. Phys. B* **100**, 93 (2010).
⁸ E. Ozbay, *Science* **311**, 189 (2006).
⁹ R. Zia, J. A. Schuller, A. Chandran, and M. L. Brongersma, *Materials Today* **9**, 20 (2006).
¹⁰ K. F. MacDonald, Z. L. Sámsón, M. I. Stockman, and N. I. Zheludev, *Nat. Photonics* **3**, 55 (2008).
¹¹ X. Huang, P. K. Jain, I. H. El-Sayed, and M. A. El-Sayed, *Nanomedicine* **2**, 681 (2007).
¹² J. Conde, G. Doria, and P. Baptista, *Journal of Drug Delivery* **2012**, 1 (2012).
¹³ K. Kneipp, H. Kneipp, I. Itzkan, R. R. Dasari, and M. S. Feld, *Chem. Rev.* **99**, 2957 (1999).
¹⁴ D. A. Genov, A. K. Sarychev, V. M. Shalaev, and A. Wei, *Nano Lett.* **4**, 153 (2004).
¹⁵ M. Li, S. K. Cushing, and N. Wu, *The Analyst* **140**, 386 (2015).
¹⁶ G. Mie, *Ann. Phys. (Leipzig)* **330**, 377 (1908).
¹⁷ B. T. Draine and P. J. Flatau, *J. Opt. Soc. Am. A* **11**, 1491 (1994).
¹⁸ W. H. Yang, G. C. Schatz, and R. P. Van Duyne, *J. Chem. Phys.* **103**, 869 (1995).
¹⁹ K. L. Kelly, E. Coronado, L. L. Zhao, and G. C. Schatz, *J. Phys. Chem. B* **107**, 668 (2003).
²⁰ N. W. Ashcroft and N. D. Mermin, *Solid State Phys.* (Saunders College, Philadelphia, 1976).
²¹ V. P. Drachev, U. K. Chettiar, A. V. Kildishev, H.-K. Yuan, W. Cai, and V. M. Shalaev, *Opt. Express* **16**, 1186 (2008).
²² P. B. Johnson and R. W. Christy, *Phys. Rev. B* **6**, 4370 (1972).
²³ R. H. Doremus, *J. Chem. Phys.* **42**, 414 (1965).
²⁴ H. Hövel, S. Fritz, A. Hilger, U. Kreibig, and M. Vollmer, *Phys. Rev. B* **48**, 18178 (1993).
²⁵ W. P. Halperin, *Rev. Mod. Phys.* **58**, 533 (1986).
²⁶ U. Kreibig and M. Vollmer, *Optical Properties of Metal Clusters* (Springer, 1995).
²⁷ A. Hilger, M. Tenfelde, and U. Kreibig, *Appl. Phys. B* **73**, 361 (2001).
²⁸ U. Kreibig and C. Fragstein, *Z. Phys. A* **224**, 307 (1969).
²⁹ U. Kreibig, *J. Phys. F* **4**, 999 (1974).
³⁰ C. Yannouleas and R. A. Broglia, *Ann. Phys. (N. Y.)* **217**, 105 (1992).
³¹ V. Bonačić-Koutecký, P. Fantucci, and J. Koutecký, *Chem. Rev.* **91**, 1035 (1991).
³² G. Galli and M. Parrinello, in *Computer Simulation in Materials Science: Interatomic Potentials, Simulation Tech-*

- niques and Applications*, edited by M. Meyer and V. Pottikis (Springer Netherlands, Dordrecht, 1991) pp. 283–304.
- ³³ J. C. Idrobo, W. Walkosz, S. F. Yip, S. Ögüt, J. Wang, and J. Jellinek, *Phys. Rev. B* **76**, 205422 (2007).
- ³⁴ V. Bonačić-Koutecky, V. Veyret, and R. Mitrić, *J. Chem. Phys.* **115**, 10450 (2001).
- ³⁵ K. Baishya, J. C. Idrobo, S. Ögüt, M. Yang, K. Jackson, and J. Jellinek, *Phys. Rev. B* **78**, 075439 (2008).
- ³⁶ C. M. Aikens, S. Li, and G. C. Schatz, *J. Phys. Chem. C* **112**, 11272 (2008).
- ³⁷ M. Kuisma, A. Sakko, T. P. Rossi, A. H. Larsen, J. Enkovaara, L. Lehtovaara, and T. T. Rantala, *Phys. Rev. B* **91**, 115431 (2015).
- ³⁸ Y. He and T. Zeng, *J. Phys. Chem. C* **114**, 18023 (2010).
- ³⁹ L. L. Jensen and L. Jensen, *J. Phys. Chem. C* **113**, 15182 (2009).
- ⁴⁰ M. Brack, *Rev. Mod. Phys.* **65**, 677 (1993).
- ⁴¹ W. A. de Heer, *Rev. Mod. Phys.* **65**, 611 (1993).
- ⁴² C. Yannouleas, E. Vigezzi, and R. A. Broglia, *Phys. Rev. B* **47**, 9849 (1993).
- ⁴³ R. A. Molina, D. Weinmann, and R. A. Jalabert, *Eur. Phys. J. D - Atomic, Molecular and Optical Physics* **24**, 127 (2003).
- ⁴⁴ G. Weick, R. A. Molina, D. Weinmann, and R. A. Jalabert, *Phys. Rev. B* **72**, 115410 (2005).
- ⁴⁵ J. Lermé, H. Baida, C. Bonnet, M. Broyer, E. Cottancin, A. Crut, P. Maioli, N. Del Fatti, F. Vallée, and M. Pellarin, *J. Phys. Chem. Lett.* **1**, 2922 (2010).
- ⁴⁶ A. Kawabata and R. Kubo, *J. Phys. Soc. Jpn.* **21**, 1765 (1966).
- ⁴⁷ F. Hache, D. Ricard, and C. Flytzanis, *J. Opt. Soc. Am. B* **3**, 1647 (1986).
- ⁴⁸ M. J. Rice, W. R. Schneider, and S. Strässler, *Phys. Rev. B* **8**, 474 (1973).
- ⁴⁹ A. A. Lushnikov and A. J. Simonov, *Phys. Lett. A* **44**, 45 (1973).
- ⁵⁰ L. Genzel, T. P. Martin, and U. Kreibig, *Z. Phys. B* **21**, 339 (1975).
- ⁵¹ R. Rupp and H. Yatom, *Phys. Status Solidi B* **74**, 647 (1976).
- ⁵² M. Cini, *J. Opt. Soc. Am.* **71**, 386 (1981).
- ⁵³ D. M. Wood and N. W. Ashcroft, *Phys. Rev. B* **25**, 6255 (1982).
- ⁵⁴ W. A. Kraus and G. C. Schatz, *J. Chem. Phys.* **79**, 6130 (1983).
- ⁵⁵ F. A. Ivanyuk, *Phys. Rev. B* **77**, 155425 (2008).
- ⁵⁶ W. C. Huang and J. T. Lue, *Phys. Rev. B* **49**, 17279 (1994).
- ⁵⁷ S. G. Rautian, *J. Exp. Theor. Phys.* **85**, 451 (1997).
- ⁵⁸ M. Barma and V. Subrahmanyam, *J. Phys. Condens. Matter* **1**, 7681 (1989).
- ⁵⁹ A. A. Govyadinov, G. Y. Panasyuk, J. C. Schotland, and V. A. Markel, *Phys. Rev. B* **84**, 155461 (2011).
- ⁶⁰ R. W. Boyd, *Nonlinear Optics: Third Edition*, 3rd ed. (Academic Press / Elsevier, 2008).
- ⁶¹ N. A. Mortensen, S. Raza, M. Wubs, T. Søndergaard, and S. I. Bozhevolnyi, *Nature Communications* **5**, 1 (2014).
- ⁶² T. V. Shahbazyan, *Phys. Rev. B* **94**, 235431 (2016).
- ⁶³ V. P. Drachev, E. N. Khaliullin, W. Kim, F. Alzoubi, S. G. Rautian, V. P. Safonov, R. L. Armstrong, and V. M. Shalaev, *Phys. Rev. B* **69**, 035318 (2004).
- ⁶⁴ M. Abramowitz and I. A. Stegun, *Handbook of Mathematical Functions: With Formulas, Graphs, and Mathematical Tables*. Edited by Milton Abramowitz and Irene A. Stegun (United States Department of Commerce, National Bureau of Standards, 1972).
- ⁶⁵ X. Li, D. Xiao, and Z. Zhang, *New J. Phys.* **15**, 023011 (2013).
- ⁶⁶ A. Hilger, *Grenzflächen-Analyse durch Mie-Plasmon-Spektroskopie an Edelmetallclustern*, Ph.D. thesis, RWTH Aachen, Aachen, Germany (2001).